Journal of Advanced Ceramics
2024, **13**(6): 821–833
https://doi.org/10.26599/JAC.2024.9220901

Research Article

A highly sensitive multiple-mode optical thermometer designed in $Eu^{2+/3+}$ and Li^{+} co-doped polymorphism compound $LaSc_3(BO_3)_4$

Nan Yang[1], Zhuo Li[1], Tingxia Zhou[1], Ziwang Zhang[1], Wen Shi[1], Yexiang Tong[1,2], Jianxin Shi[1]✉

[1] *School of Chemistry, IGCME, Sun Yat-sen University, Guangzhou 510006, China*
[2] *MOE of the Key Laboratory of Bioinorganic and Synthetic Chemistry, IGCME, The Key Lab of Low-Carbon Chemistry & Energy Conservation of Guangdong Province, Sun Yat-sen University, Guangzhou 510006, China*

Received: March 6, 2024; Revised: April 7, 2024; Accepted: April 23, 2024

Abstract: Noncontact optical thermometers have attracted widespread attention, but existing problems such as single-mode and low-sensitivity thermometers still urgently need to be solved. Herein, a novel multiple-mode thermometer was designed for the polymorphism $LaSc_3(BO_3)_4$:$Eu^{2+/3+}$,Li^{+}. X-ray diffraction (XRD) patterns revealed a slight transition between α- and β-phases with the concentrations of the dopants, which is further proved by structure refinements and first-principles calculations. The coexistence of Eu^{2+} and Eu^{3+} in the phosphors and their relative percentages were confirmed by X-ray absorption near-edge structure (XANES) spectra. Benefiting from appropriate emissions from Eu^{2+} and Eu^{3+} without obvious energy transfer and their opposite changing trends with temperatures under 307 nm excitation, a triple-mode optical thermometer is obtained for this material within the temperature range of 150–450 K. The highest sensitivities of 27.65, 14.05, and 7.68 %·K^{-1} are achieved based on two fluorescence intensity ratio (FIR) modes of Eu^{2+} and Eu^{3+} ($5d–4f/^5D_0–^7F_{2,4}$) and the fluorescence lifetime (FL) mode of Eu^{2+}, respectively. To the best of our knowledge, the former is almost the highest in Eu^{2+} and Eu^{3+} co-doped thermometers. These results indicate that this material may be used as an excellent multiple-mode optical thermometer.

Keywords: europium (Eu) ions; phase transition; multiple-mode optical thermometer; thermal quenching properties; fluorescence intensity ratio (FIR); fluorescence lifetime (FL)

1 Introduction

Temperature, a crucial thermodynamic parameter, not only influences daily life but also plays important roles in industrial production, scientific surveys, and many other fields [1–3]. To meet the demands for highly accurate and sensitive temperature measurements, exploring thermometers with excellent performance has attracted widespread attention [4–6]. Conventional thermometers based on the thermal expansion and contraction characteristics of liquids or metals have difficulty avoiding direct contact with targets [7,8]. Therefore, it is difficult to satisfy the measurement requirements under many harsh conditions, such as extreme temperatures and strong corrosion [9,10]. To overcome these difficulties, noncontact optical thermometers, which depend on the real-time response of the temperature-dependent optical properties of rare earth or other metal ions, have become popular due to their advantages of high sensitivity, rapid response, high spatial resolution, etc. [11–13]. The abundant optical properties of luminescent materials, including fluorescence emission intensity, emission peak position, bandwidth, band shape, and fluorescence lifetime, show close relationships with temperatures, which provides important bases for optical temperature measurements [14–16].

To date, fluorescence intensity ratio (FIR) and fluorescence lifetime (FL) have become the two most commonly investigated parameters used for temperature monitoring [17,18]. FIR-based thermometers are generally divided into two kinds: those with thermally coupled energy levels and those with nonthermally coupled energy levels [19]. The former must meet the requirement of an appropriate energy difference of 200–2000 cm^{-1}, which greatly impedes the improvement of sensitivity and the enhancement of accuracy [20]. In contrast, the latter utilizes the regular and significant temperature responses of dual-luminescent centers without energy limitations, so it can not only effectively avoid interference from external factors but also contribute to widening the temperature range and increasing the temperature sensitivity [21]. The FL-based method experiences fewer uncertainties arising from light sources or measurement conditions compared with the FIR-based technique, but the equipment is relatively more expensive, and the working temperature is not flexible [22]. Many luminescent materials, such as $YNbO_4$:Yb^{3+}/Er^{3+} nanoparticles, $LaPO_4$:Yb^{3+}/Nd^{3+} nanourchins, and Sr_2InTaO_6:Mn^{4+} phosphors, have been used in FIR- or FL-based thermometers [23–25]. However, most of the reports only focus on single-mode temperature sensing techniques, which possibly induce some deviations due to insensitivity in certain temperature regions [8,18]. Therefore, developing dual- or multiple-mode thermometers is highly important for increasing the measurement accuracy. Recently, $Ca_3LiZnV_3O_{12}$:Sm^{3+} phosphors have been reported as four-mode luminescent thermometers with maximal relative sensitivities of 2.41 %·K^{-1} (342 K) based on fluorescence intensity, 1.91 %·K^{-1} (336 K) based

✉ Corresponding author.
E-mail: cessjx@mail.sysu.edu.cn

清華大學出版社 Tsinghua University Press | SciOpen

on FIR, 0.567 %·K^{-1} (303 K) based on the Commission Internationale de L'Eclairage (CIE) coordinates, and 1.27 %·K^{-1} (303 K) based on the excitation intensity ratio [26]. $Ca_3LiMgV_3O_{12}$:Sm^{3+} and $LnP_{0.5}V_{0.5}O_4$:Er^{3+}/Yb^{3+} (Ln = Y, Gd, and La) phosphors have also been reported as triple- and dual-mode thermometers with maximal relative sensitivities of 1.99 %·K^{-1} (357 K) and 1.05 %·K^{-1} (300 K), respectively [27,28]. Although remarkable progress has been made in multiple-mode thermometers, the sensitivity and thermometry range still need to be further improved to meet the demands of practical applications.

As a typical rare earth element, europium (Eu) may be a suitable activator of phosphors for noncontact luminescent thermometers. Both Eu^{2+} and Eu^{3+} are often used as luminescent centers, but their luminescence properties are quite different. Eu^{2+} is known for its $4f^7$ electron configuration and generally exhibits broadband emission arising from the parity-allowed $4f^65d^1$–$4f^7$ transition [29]. Due to the exposed 5d excited-state outer orbital, the emission of Eu^{2+} is easily affected by the host lattice environment and coordination conditions [30]. Unlike Eu^{2+}, Eu^{3+} possesses a stable $4f^6$ electronic configuration, and several sharp peaks in its emission are attributed to parity-forbidden 4f–4f transitions [31–33]. The luminescence of Eu^{3+} is basically undisturbed by the external environment due to the shielding of the outer $5s^2$ and $5p^6$ electrons, so Eu^{3+} is an appropriate internal reference in optical thermometers [34,35]. Therefore, Eu^{2+}- and Eu^{3+}-co-doped phosphors are proposed to be ideal temperature-sensing materials [35]. However, the selection of hosts and the synthesis conditions for mixed-valence phosphors should meet specific requirements, such as an appropriate reducing atmosphere, coordination environment, and lattice size, which can hinder the preparation of such materials [36,37]. There are several reports on Eu^{2+} and Eu^{3+} co-doped phosphors for the temperature measurement, such as $Eu^{2+/3+}$ co-doped $Sr_{1.95+x}Li_{1-x}Si_{1-x}Al_xO_4F$ ($0 \le x \le 0.25$) [36], $Sr_3P_4O_{13}$ [38], and $MgAl_2O_4$ [39]. However, only the FIR-based technique has been adopted, and the relative sensitivities of 0.83, 1.06, and 0.83 %·K^{-1} are not satisfactory.

Optical thermometry is currently considered a valuable research field. However, most researchers have focused on pure-phase materials in this field, and they are likely to ignore the improvement in the performance induced by structure–phase transitions in mixed-phase materials. In fact, not all inorganic compounds are easily prepared with a pure phase, and materials with structure-phase transitions, such as the electrostatic-doping-driven phase transition in monolayer molybdenum ditelluride ($MoTe_2$) [40] and temperature-induced structural transition in a photoluminescent thermometer of $Na[(Gd_{0.8}Eu_{0.1}Tb_{0.1})SiO_4]$, may have regular and excellent optical, electrical, or magnetic properties [41]. Unfortunately, relatively few investigations on multiphase materials for optical thermometry have been reported. Therefore, it is of theoretical significance and application value to explore optical thermometers based on multiphase materials co-activated with Eu^{2+} and Eu^{3+}.

In our previous work [42], Eu^{3+}-doped polymorphic $LaSc_3(BO_3)_4$ (denoted LSBO) phosphors were studied in detail, and the thermal stability of the resulting luminescence was shown to be excellent. More importantly, increasing the doping concentration of Eu^{3+} from 0 to 0.80 has been proven to induce the phase transition from α to β and improve the luminescence of Eu^{3+} in the LSBO. Herein, Eu^{2+} and Eu^{3+} co-doped LSBO polymorphism with Li^+ as a charge compensation agent is chosen to obtain a multiple-mode optical thermometer with high sensitivity. Similar to our previous report, the doping of $Eu^{2+/3+}$ or Li^+ can induce the slight transformation of the LSBO phase from α to β. The phase percentages with different concentrations of $Eu^{2+/3+}$ and Li^+ were confirmed by two-phase X-ray diffraction (XRD) refinements, and the phase transition process was explained by the total energy of the system based on first-principles calculations. As the phase transforms from α to β, the percentage of Eu^{2+} increases, which is proven by the XANES spectra. According to the refinements of the temperature-dependent XRD patterns, the phase percentage and crystal structure can hardly be influenced by the temperature within 200–600 K, which provides a good foundation for this material to serve as an optical thermometer. The temperature-dependent emission spectra under 307 nm excitation showed that the changes in the emission intensities of Eu^{2+} and Eu^{3+} were opposite within the temperature range of 150–450 K. Three modes, including two FIR-based and one FL-based mode, were detected in this material, and the highest relative sensitivities of FIR_1 (5d–4f/$^5D_0$–$^7F_2$), FIR_2 (5d–4f/$^5D_0$–$^7F_4$), and the FL of Eu^{2+} reached 27.65, 14.05, and 7.68 %·K^{-1}, respectively. The minimum values of their temperature resolutions are 0.0004, 0.0007, and 0.018 K. Compared with recent reports, the relative sensitivities of this work show apparent advantages, giving great potential for application in optical thermometry.

2 Experimental

2.1 Raw materials and sample preparation

Two series of $La_{1-x}Sc_3(BO_3)_4$:$xEu^{2+/3+}$ (x = 0, 0.02, 0.04, 0.06, 0.08, and 0.10) and $La_{0.98}Sc_3(BO_3)_4$:0.02$Eu^{2+/3+}$,yLi^+ (y = 0.02, 0.05, 0.08, 0.10, 0.15, and 0.20) samples were prepared via a high-temperature solid-state method. The raw materials, including La_2O_3 (99.99%), Sc_2O_3 (99.99%), H_3BO_3 (99.99%), Eu_2O_3 (99.99%), and Li_2CO_3 (99.99%), were mixed in an agate mortar according to stoichiometric ratios, and 20% excess H_3BO_3 was added to the mixtures. After being thoroughly ground for more than 20 min, the mixtures were transferred into an alumina crucible and preheated at 873 K for 3 h in an air atmosphere with a heating rate of 5 K·min^{-1}. Then, the mixtures were reground and heated at 1573 K for 5 h under a reducing atmosphere containing 5% H_2 and 95% N_2. After naturally cooling to room temperature, the synthesized samples were reground for subsequent measurements.

2.2 Measurements and characterizations

Powder X-ray diffraction (PXRD) data at room temperature for the phase characterization and crystal structure analysis were collected on a diffractometer (D-Max 2200 VPC, Rigaku) at 40 kV and 26 mA with Cu Kα radiation (λ = 1.5405 Å). The temperature-dependent XRD data were measured with a diffractometer (D8 Advance, Bruker) with Cu Kα radiation (λ = 1.5405 Å). The XRD data were collected with the JADE 6 software. The XRD refinements were conducted with the GSAS software [43]. The morphology and elemental composition of the samples were analyzed on a scanning electron microscope (SEM; Quanta, FEI) equipped with an energy-dispersive spectrometer. X-ray absorption spectra at the Eu L_3-edge XANES were collected at beamline BL14W1 of the Shanghai synchrotron radiation facility (SSRF) using a Lytle detector with a Cr filter. The measurements were performed at room temperature, and the excitation energies were selected by a Si(111) double-crystal monochromator. Photoluminescence excitation (PLE) and emission (PL) spectra were measured by a fluorescence spectrophotometer (FLS980,

Edinburgh Instruments Ltd.) equipped with a 450 W xenon lamp and a 345 nm laser. With the help of an additional Oxford OptistatDN temperature controller, temperature-dependent PL spectra and decay curves within the temperature range of 150–450 K were collected on the same instrument.

2.3 Calculations of system total energy

Considering that each unit cell of α- and β-LSBO encompasses 4 and 3 chemical formulas of $LaSc_3(BO_3)_4$, respectively, 3 × 1 × 1 and 2 × 2 × 1 supercells were individually constructed for α- and β-LSBO. The total number of atoms in the simulated supercells is 240, incorporating 12 La^{3+} sites. Predicated upon the supercell structures of each phase of the LSBO, we randomly substituted one Eu^{2+} and one Eu^{3+} for two La^{3+} sites to create the LSBO:$Eu^{2+/3+}$ doping model. Subsequently, one Li^+ ion was placed on the basis of this doping model to obtain the novel structure of LSBO:$Eu^{2+/3+}$,Li^+. All the structures thus established were optimized, and their respective total energies were obtained.

The structural optimizations were performed by the projector augmented wave (PAW) method [44] with the Perdew–Burke–Ernzerhof (PBE) exchange-correlation functional [45] in the Vienna *ab initio* simulation package (VASP) (version 6.2.1) [46]. Monkhorst–Pack *k*-point meshes of 1 × 2 × 2 and 1 × 1 × 3 were used for the α- and β-phases, respectively, during the structural optimizations. The cutoff energy for the plane-wave basis set was 320 eV. The convergence criterion for the total energy was set to 10^{-4} eV, and the residual force on each atom should be smaller than 0.05 eV·Å^{-1}. For the system total energy calculations, *k*-points of 1 × 4 × 4 and 1 × 1 × 6 Monkhorst–Pack grids were used for the α- and β-phases, respectively. Moreover, the cutoff energy for the plane-wave basis set was 500 eV. The convergence criterion for the total energy was set to 10^{-5} eV.

3 Results and discussion

3.1 Structure and composition analyses

LSBO crystals were reported to be polymorphic compounds with different phases, including the α- and β-phases [47–49]. As presented in Fig. 1(a), the α-LSBO crystal belongs to the *C*12/*c*1 space group (ICSD#83404). The [ScO_6] octahedra connect with each other by sharing edges, generating pieces of twisty chains. The [LaO_6] octahedra and [BO_3] triangles connect with [ScO_6]

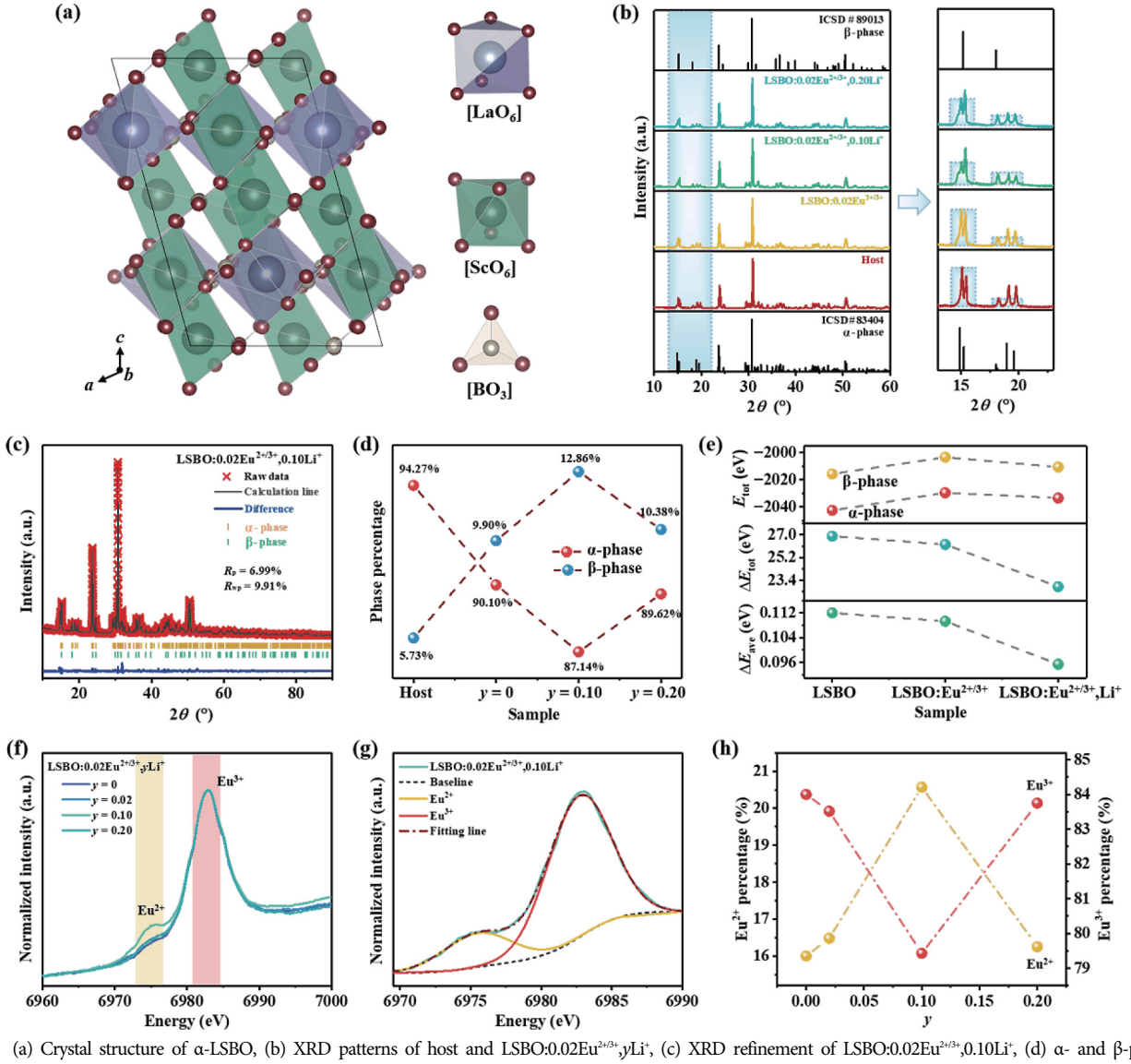

Fig. 1 (a) Crystal structure of α-LSBO, (b) XRD patterns of host and LSBO:0.02$Eu^{2+/3+}$,*y*Li^+, (c) XRD refinement of LSBO:0.02$Eu^{2+/3+}$,0.10Li^+, (d) α- and β-phase percentages of host and LSBO:0.02$Eu^{2+/3+}$,*y*Li^+, (e) calculated E_{tot}, ΔE_{tot}, and ΔE_{ave} of LSBO, LSBO:$Eu^{2+/3+}$, and LSBO:$Eu^{2+/3+}$,Li^+, (f) Eu L_3-edge XANES spectra of LSBO:0.02$Eu^{2+/3+}$,*y*Li^+, (g) peak fitting for XANES spectra of LSBO:0.02$Eu^{2+/3+}$,0.10Li^+, and (h) relative percentages of Eu^{2+} and Eu^{3+} in LSBO:0.02$Eu^{2+/3+}$,*y*Li^+.

清華大学出版社 Tsinghua University Press | SciOpen

octahedra by sharing angles, forming a low-symmetry monoclinic phase. The crystal structure of β-LSBO shown in Fig. S1 in the Electronic Supplementary Material (ESM) is similar to that of α-LSBO, but it belongs to the trigonal *R*32 space group with greater symmetry (ICSD#89013). It is clear from the crystal parameters listed in Tables S1 and S2 in the ESM that the atomic surroundings in the α-phase are more complex than those in the β-phase. Therefore, the phase transition of the prepared samples can be easily distinguished from the XRD patterns.

The XRD patterns of the host and LSBO:0.02$Eu^{2+/3+}$,*y*Li^+ (*y* = 0, 0.10, and 0.20) are shown in Fig. 1(b). An enlarged image of Fig. 1(b) clearly shows that the intensities of the peaks corresponding to the α-phase gradually decrease while those corresponding to the β-phase increase, which implies a phase transition from α to β with the doping of $Eu^{2+/3+}$ or Li^+. However, when *y* is greater than 0.10, the percentage of the β-phase decreases (Fig. S2 in the ESM). Due to the coexistence of the two phases, XRD refinements were conducted to further identify the percentage of each phase. The refinement of LSBO:0.02$Eu^{2+/3+}$,0.10Li^+ in Fig. 1(c) shows that the final reliability factors of R_p and R_{wp} are low enough, and no other evident impurities exist in the sample. The refined results of the other samples are shown in Fig. S3 and Table S3 in the ESM. All the peaks corresponded well with the standards of ICSD#83404 and 89013, and the good fitting parameters demonstrated the satisfactory phase purity of the as-prepared samples. The cell parameters in Table S3 in the ESM show that the values of *a*, *b*, *c*, and *V* decrease with increasing $Eu^{2+/3+}$ doping. After codoping Li^+, the values of *a*, *b*, *c*, and *V* first decrease and then increase when the content of Li^+ is greater than 0.10. The change trend of the percentage of the β-phase is opposite to this according to the two-phase refined results shown in Fig. 1(d). Since the cell volume of the β-phase is evidently smaller than that of the α-phase, as recorded in Tables S1 and S2 in the ESM, an increase in the β-phase will lead to a decrease in *V*.

To further explain the phase transition induced by doping with $Eu^{2+/3+}$ and Li^+, the total energies of α- and β-LSBO:$Eu^{2+/3+}$,Li^+ were estimated by first-principles calculations. As presented in Fig. 1(e), the system total energy (E_{tot}) of α-LSBO:$Eu^{2+/3+}$,Li^+ is always lower than that of β-LSBO:$Eu^{2+/3+}$,Li^+, implying that α-LSBO:$Eu^{2+/3+}$,Li^+ is easier to form. As shown in Fig. 1(d), the percentage of α-LSBO:$Eu^{2+/3+}$,Li^+ is greater than that of β-LSBO:$Eu^{2+/3+}$,Li^+ under similar doping conditions. However, it is also worth noting the system total energy discrepancy (ΔE_{tot}) and average energy discrepancy per atom (ΔE_{ave}), because the two phases tend to form simultaneously when the discrepancy is small enough. Compared to those of undoped LSBO, the values of ΔE_{tot} and ΔE_{ave} gradually decrease after doping with $Eu^{2+/3+}$ and Li^+, which contributes to understanding the phase transition from α to β.

Because the radii of Eu^{2+} (*r* = 1.17 Å, CN = 6, where CN is the coordination number) and Eu^{3+} (*r* = 0.947 Å, CN = 6) are closer to that of La^{3+} (*r* = 1.032 Å, CN = 6) compared with Sc^{3+} (*r* = 0.745 Å, CN = 6), the doped Eu^{2+} and Eu^{3+} ions are considered to prefer to occupy the sites of La^{3+} [50]. To further confirm this point, the radius percentage difference (D_r) and the bond energy difference (ΔE) between the dopants (Eu^{2+} or Eu^{3+}) and the possible replaced ions (La^{3+} or Sc^{3+}) were calculated, and the results are shown in Tables S4 and S5 in the ESM, respectively. The D_r and ΔE values for the pairs of $Eu^{2+/3+}$–La^{3+} are always much smaller than those for the pairs of $Eu^{2+/3+}$–Sc^{3+}, implying that both Eu^{2+} and Eu^{3+} are more likely to replace La^{3+} rather than Sc^{3+} in LSBO.

The SEM images and energy dispersive X-ray spectroscopy (EDS) elemental mappings of LSBO:0.02$Eu^{2+/3+}$,0.10Li^+ in Fig. S4 in the ESM show that the sample particles have irregular geometric shapes with an average diameter of approximately 15 μm, and the elements La, Sc, and Eu are uniformly dispersed in the as-prepared sample, which illustrates the successful doping of $Eu^{2+/3+}$. Table S6 in the ESM shows the atomic percentage of LSBO:0.02$Eu^{2+/3+}$,0.10Li^+, and the metal elemental composition is basically in accordance with the stoichiometric ratio, suggesting the successful synthesis of LSBO:0.02$Eu^{2+/3+}$,0.10Li^+.

To further verify the coexistence of mixed-valence Eu, the XANES spectra of LSBO:0.02$Eu^{2+/3+}$,*y*Li^+ (*y* = 0, 0.02, 0.10, and 0.20) were obtained, and their Eu L_3-edge spectra are shown in Fig. 1(f). Two peaks at approximately 6975 and 6983 eV can be observed, which correspond to the transitions from $2p_{3/2}$ to 5d of Eu^{2+} and Eu^{3+}, respectively [51]. The relative percentages of Eu^{2+} and Eu^{3+} in LSBO:0.02$Eu^{2+/3+}$,0.10Li^+ are determined to be 20.57% and 79.43%, respectively, by peak fitting, as shown in Fig. 1(g). The results for the other samples are shown in Fig. S5 and Table S7 in the ESM. The percentage of Eu^{2+} in LSBO:0.02$Eu^{2+/3+}$,0.10Li^+ is the highest, while in LSBO:0.02$Eu^{2+/3+}$ is the lowest, as depicted in Fig. 1(h).

3.2 Photoluminescence properties of LSBO:$Eu^{2+/3+}$ and LSBO:$Eu^{2+/3+}$,Li^+

The PLE and PL spectra of LSBO:0.02$Eu^{2+/3+}$ are shown in Fig. 2(a). Under excitation at 310 nm, there is a broad band from 350 to 650 nm and four sharp peaks at 590, 616, 652, and 701 nm in the PL spectra, which are ascribed to the $4f^65d^1$–$4f^7$ transition of Eu^{2+} and the $^5D_0$–^7F_J (*J* = 1, 2, 3, and 4) transitions of Eu^{3+}, respectively. When the emission at 430 nm was monitored, only a broad band at 240–400 nm attributed to Eu^{2+} was detected. At 616 nm, a broad band within 235–335 nm and several sharp peaks at 361, 375, 380, 394, 414, and 465 nm are detected, which are the charge transfer bands of O^{2-}–Eu^{3+} and the 4f–4f transitions of Eu^{3+} from its $^7F_0$ ground state to the excited states, including $^5D_4$, $^5G_4$, $^5G_2$, $^5L_6$, $^5D_3$, and $^5D_2$, respectively. Although the PLE spectrum of Eu^{3+} overlaps with the PL spectrum of Eu^{2+} from 350 to 480 nm, the characteristic excitation peak of Eu^{2+} is not observed when the emission at 616 nm is monitored, which means that there is no obvious energy transfer between Eu^{2+} and Eu^{3+}. A similar phenomenon has been reported for Eu^{2+} and Eu^{3+} co-doped Sc_2O_3 nanoparticles, which may contribute to the high reliability of temperature monitoring [35]. The schematic energy-level diagram of LSBO:$Eu^{2+/3+}$ presented in Fig. 2(b) can be used to explain the excitation and emission processes of the phosphors.

Because the luminescence of Eu^{2+} is sensitive to its environment, the excitation wavelength of 340 nm, where Eu^{3+} has no obvious absorption, was selected for further analysis. As presented in the middle of Fig. 2(a), the broadband emission ascribed to the 5d–4f transition of Eu^{2+} is clearly observed, whose full width at half-maximum is approximately 77 nm. Figure 3(a) shows the concentration-dependent PL spectra of LSBO:*x*$Eu^{2+/3+}$. The emission intensity first increases until *x* reaches 0.02 and then decreases with further increases in the *x* value due to the concentration quenching effect. Since the emission spectra are obviously asymmetric, Gaussian fitting of LSBO:0.02$Eu^{2+/3+}$ with two peaks belonging to the α- and β-phases was conducted, and the results are shown in Fig. 3(b). According to Dorenbos's studies, the crystal field strength (ε_{cfs}) has a negative correlation with the average bond length of cation sites (R_{ave}), which is expressed as Eqs. (1) and (2) [52,53]:

$$\varepsilon_{cfs} = \beta_{poly}/R_{ave}^2 \quad (1)$$

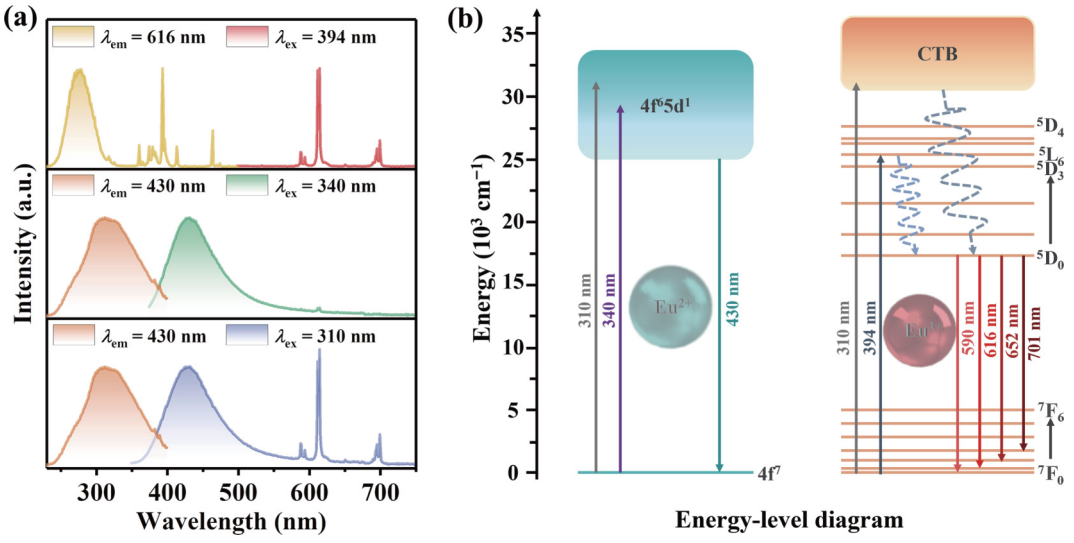

Fig. 2 (a) PLE and PL spectra of LSBO:0.02$Eu^{2+/3+}$ monitored at different emission wavelengths and with different excitations and (b) schematic energy-level diagram of LSBO:$Eu^{2+/3+}$.

$$R_{ave} = \frac{1}{n}\sum_{i=1}^{n}(R_i - 0.6\Delta R) \quad (2)$$

where β_{poly} is a constant related to the type of coordination polyhedron; n refers to the coordination number of the Eu^{2+} ion; R_i represents the bond length between Eu^{2+} and the coordination anions, and ΔR refers to the difference in the ionic radii between Eu^{2+} and La^{3+}. On the basis of Eq. (2), R_{ave} of La^{3+} is calculated to be 2.388 Å in the α-phase and 2.400 Å in the β-phase (Table S8 in the ESM). Due to the very small difference in R_{ave} between the α- and β-phases, the effect of the next nearest neighboring ions is taken into consideration. As depicted in Fig. S6 in the ESM, three [ScO_6] octahedra connect with each other via common edges and points in the α- and β-phases, respectively. Then, they connect with the La atom by sharing oxygen atoms and forming a closed ring. The bond lengths of [ScO_6] octahedra in the α- and β-phases are summarized in Table S9 in the ESM, and the average bond lengths are calculated to be approximately 2.1 and 2.2 Å, respectively. Clearly, the average bond length of [ScO_6] octahedra in the β-phase is greater than that in the α-phase. Therefore, the [LaO_6] octahedra in the β-phase receive more pressure from [ScO_6] octahedra, which leads to more distorted and shrunken [LaO_6] polyhedra in the β-phase and results in greater crystal-field splitting. A stronger crystal field results in a lower emission energy. Therefore, the emission at 2.65 eV shown in Fig. 3(b) is attributed to the β-phase. With increasing x from 0.01 to 0.05, an evident redshift in the emission from 420 to 447 nm can be easily observed in Fig. 3(c), and the fitting emissions for the α- and β-phases shift from 418 to 444 nm and from 460 to 490 nm, respectively. The reasons will be explained later.

Due to the imbalanced charge after the substitution of La^{3+} with Eu^{2+}, Li^+ ions are co-doped to compensate for the charge. The PLE and PL spectra of LSBO:0.02$Eu^{2+/3+}$,0.10Li^+ shown in Fig. S7 in the ESM are very similar to those of LSBO:0.02$Eu^{2+/3+}$ in Fig. 2(a), but the optimal excitation and emission wavelengths slightly shift. The strongest excitation wavelength of Eu^{2+} in LSBO:0.02$Eu^{2+/3+}$,0.10Li^+ shifts to 307 nm, while the emission wavelength moves to 455 nm. As presented in Fig. 3(d), the emission intensity of LSBO:0.02$Eu^{2+/3+}$,$y$$Li^+$ becomes greater as the concentration of Li^+ increases to y = 0.10, and then it gradually weakens with increasing concentrations of Li^+, which is similar to the results from XANES of the Eu L_3-edge. The reason may be that Li^+ is easily evaporable during the preparation process. Thus, excessive amounts are more appropriate. However, the charge is still difficult to balance, and even more defects may be generated if the Li^+ concentration is too high. The internal quantum efficiencies (IQEs) of LSBO:0.02$Eu^{2+/3+}$ and LSBO:0.02$Eu^{2+/3+}$,0.10Li^+ shown in Fig. S8 in the ESM are 16.0% and 21.1%, respectively. The results of Gaussian fitting of LSBO:0.02$Eu^{2+/3+}$,0.10Li^+ are presented in Fig. 3(e). The effect of the codoping of Li^+ on the environment of Eu^{2+} in the two phases is almost the same. Therefore, the two emissions located at 2.74 and 2.49 eV in Fig. 3(e) should belong to the α- and β-phases, respectively. Compared with that of LSBO:0.02$Eu^{2+/3+}$ in Fig. 3(b), the emission of LSBO:0.02$Eu^{2+/3+}$,$y$$Li^+$ shifts to a lower energy, as described in Fig. 3(f).

The redshift of the emission of Eu^{2+} mentioned above can be explained by the environmental changes in the [EuO_6] octahedra induced by the increased doping concentration of $Eu^{2+/3+}$ or Li^+ and the phase transition between α and β. The schematic diagrams depicted in Fig. 4 can be used to understand these redshift phenomena. (i) Because Eu^{2+} and Eu^{3+} coexist in LSBO:$Eu^{2+/3+}$ phosphors and their radii are very close to that of La^{3+}, it is difficult to estimate the changes in [LaO_6] octahedra with and without the substitution of $Eu^{2+/3+}$. However, the phase transition from α to β was confirmed after doping with $Eu^{2+/3+}$, and V was accordingly reduced. Moreover, the calculated R_{ave} values of [LaO_6] octahedra in α- and β-LSBO in Table S8 in the ESM are very close, and the numbers of [LaO_6] octahedra in a unit cell, Z, for LSBO:0.02$Eu^{2+/3+}$,$y$$Li^+$ in Table S10 in the ESM do not show any obvious changes. These results will lead to an increase in the pressure exerted on [EuO_6] octahedra as more $Eu^{2+/3+}$ ions are introduced, and [EuO_6] octahedra tend to shrink and distort, resulting in an increase in the crystal field splitting energy and emission shifting toward longer wavelengths. (ii) When Li^+ is added to LSBO:0.02$Eu^{2+/3+}$, not only does the LSBO phase further transfer from α to β, but additional Li^+ ions also squeeze [EuO_6], which leads to greater crystal field splitting and a redshift in the emission of Eu^{2+}. When the doping concentration of Li^+ is greater than 0.10, the phase transfer from β to α and V increases. On account of this point, the received pressure of [EuO_6] in LSBO:0.02$Eu^{2+/3+}$,0.20Li^+ weakens, and the emission slightly blueshifts, as depicted in Fig. 3(f).

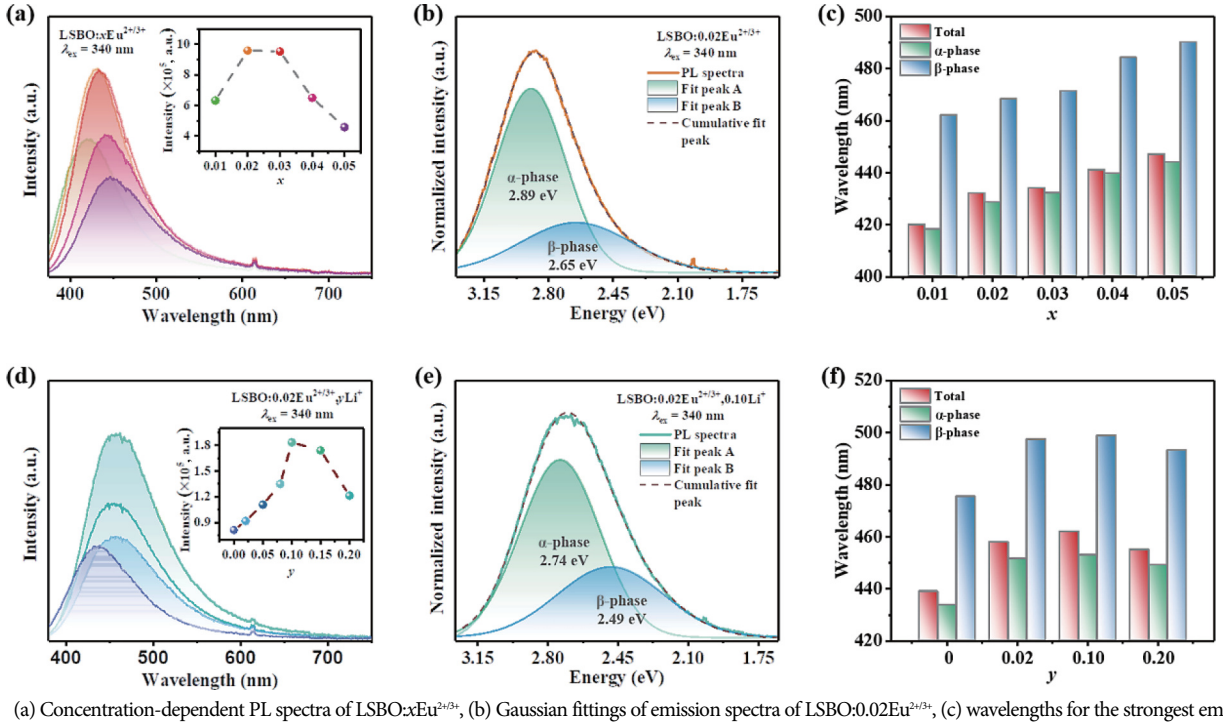

Fig. 3 (a) Concentration-dependent PL spectra of LSBO:xEu$^{2+/3+}$, (b) Gaussian fittings of emission spectra of LSBO:0.02Eu$^{2+/3+}$, (c) wavelengths for the strongest emission of total, α- and β-LSBO:xEu$^{2+/3+}$, (d) PL spectra of LSBO:0.02Eu$^{2+/3+}$,yLi$^+$, (e) Gaussian fittings of emission spectra of LSBO:0.02Eu$^{2+/3+}$,0.10Li$^+$, and (f) wavelengths for the strongest emission of total-, α-, and β-LSBO:0.02Eu$^{2+/3+}$,yLi$^+$.

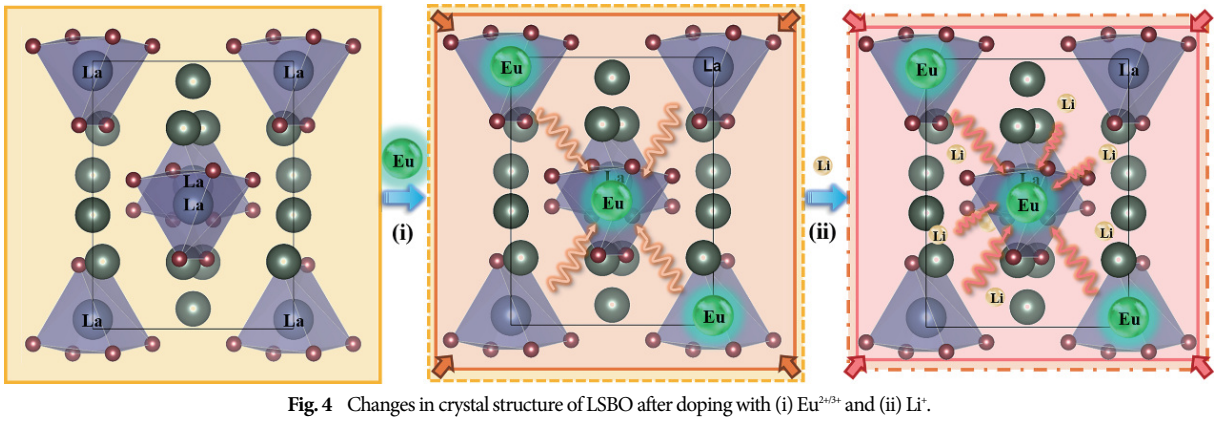

Fig. 4 Changes in crystal structure of LSBO after doping with (i) Eu$^{2+/3+}$ and (ii) Li$^+$.

3.3 Thermal stability and optical properties of LSBO:0.02Eu$^{2+/3+}$,0.10Li$^+$

Figure 5(a) shows the temperature-dependent XRD patterns of LSBO:0.02Eu$^{2+/3+}$,0.10Li$^+$. From 200 to 600 K, the position, shape, and intensity of the XRD peaks do not change significantly, which illustrates that the crystal structure of the phosphor remains almost unchanged. The refinements of LSBO:0.02Eu$^{2+/3+}$,0.10Li$^+$ at 200 and 600 K are presented in Figs. 5(b) and 5(c), respectively, and the final reliability factors are low enough. The refined results of the XRD patterns measured at other temperatures shown in Fig. S9 in the ESM are also satisfactory, revealing the inconspicuous variation in the crystal structures at different temperatures. The refined results summarized in Table S11 in the ESM show that the percentages of the two phases at various temperatures are essentially the same, which further indicates that the temperature will not significantly affect the crystal structure of the LSBO.

To study the thermal quenching properties of LSBO:0.02Eu$^{2+/3+}$, 0.10Li$^+$, the temperature-dependent PL spectra were measured and are shown in Fig. 6(a). Under the excitation at 307 nm, the shape of the broadband emission belonging to Eu^{2+} at various temperatures was almost unchanged, but the intensity decreased rapidly. However, the emission intensities at 590, 616, 652, and 701 nm correspond to the $^5D_0$–^7F_J (J = 1, 2, 3, and 4) transitions of Eu^{3+} increase continuously. This abnormal thermal quenching of Eu^{3+} can be explained by the edge abnormal thermal quenching effect found in LSBO:0.02Eu^{3+} (Fig. S10 in the ESM), and similar phenomena have been observed in $CaMoO_4$, $CaWO_4$, $LuVO_4$, Gd_3TaO_7, etc. [54–56]. At 450 K, the emission intensity of the 5d–4f transition of Eu^{2+} is evidently lower than that of $^5D_0$–$^7F_2$ or $^5D_0$–$^7F_4$ of Eu^{3+}, which is obviously contrary to that at 150 K, as presented in Fig. 6(b). The significant difference in thermal quenching between Eu^{2+} and Eu^{3+} in LSBO:0.02Eu$^{2+/3+}$,0.10Li$^+$ can account for the evident color shift from cyan to blue and pink, as shown in Fig. 6(c), which indicates that the phosphor may have great potential for applications in optical thermometry.

Therefore, the ratio between the emission intensity of the 5d–4f transition and the $^5D_0$–$^7F_2$ or $^5D_0$–$^7F_4$ transition was used to calculate FIR. As shown in Figs. 6(d) and 6(g), the calculated values of FIR$_1$ (5d–4f/$^5D_0$–$^7F_2$) and FIR$_2$ (5d–4f/$^5D_0$–$^7F_4$) decrease monotonically with increasing temperature. The experimental

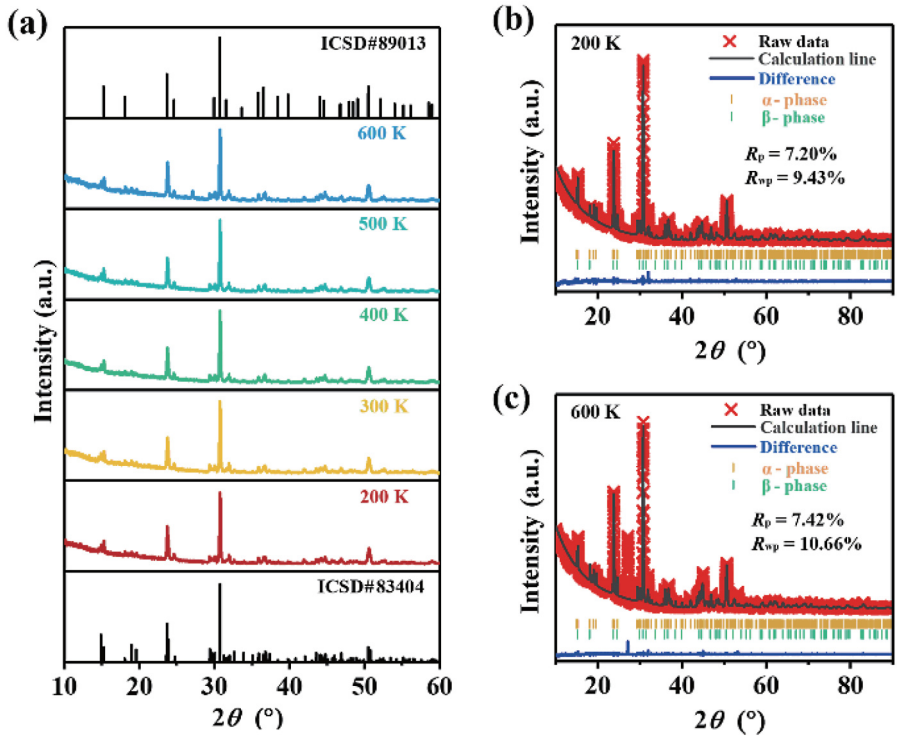

Fig. 5 (a) Temperature-dependent XRD patterns of LSBO:0.02$Eu^{2+/3+}$,0.10Li^{+} from 200 to 600 K and LSBO:0.02$Eu^{2+/3+}$,0.10Li^{+} refinements at (b) 200 K and (c) 600 K.

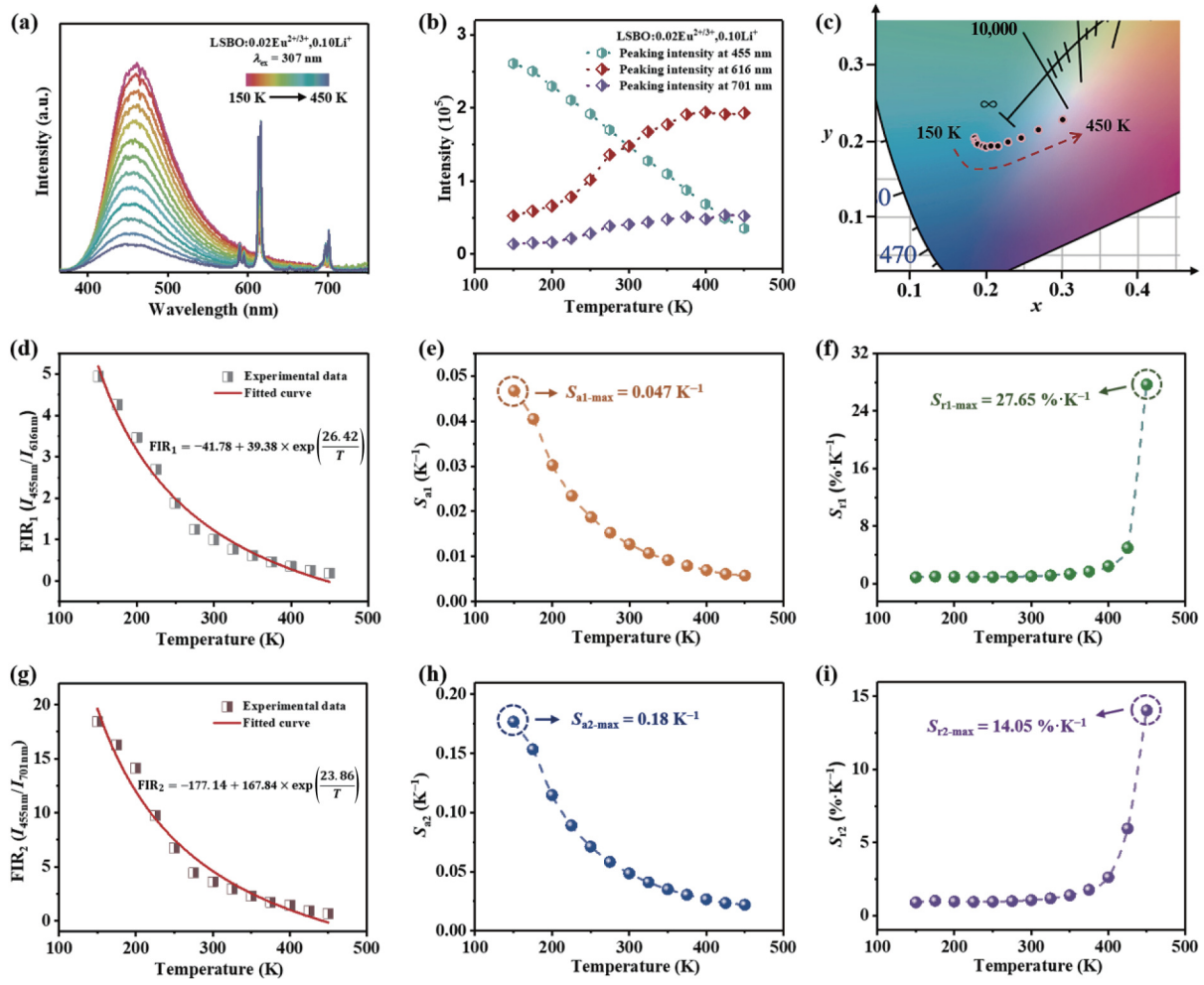

Fig. 6 (a) Temperature-dependent PL spectra of LSBO:0.02$Eu^{2+/3+}$,0.10Li^{+} from 150 to 450 K, (b) intensity change trends of emissions at 455, 616, and 701 nm, (c) CIE coordinates, (d) calculated FIR_1 values and fitted curve, (e) corresponding S_{a1} values, (f) corresponding S_{r1} values, (g) calculated FIR_2 values and fitted curve, (h) corresponding S_{a2} values, and (i) corresponding S_{r2} values.

清華大学出版社 Tsinghua University Press | SciOpen

data can be expressed as Eq. (3) (see Table S12 and Fig. S11 in the ESM) [57,58]:

$$\mathrm{FIR} = \frac{I_{Eu^{2+}}}{I_{Eu^{3+}}} = A + B\exp\left(-\frac{C}{T}\right) \quad (3)$$

where $I_{Eu^{2+}}$ and $I_{Eu^{3+}}$ are emission intensities of Eu^{2+} and Eu^{3+} activators, A, B, and C are related constant parameters, and T is the absolute temperature. With mathematical fitting by Eq. (3), both FIR_1 and FIR_2 can be obtained and are presented in Figs. 6(d) and 6(g).

To quantitatively evaluate the performance of the optical thermometer, the absolute temperature sensitivity (S_a) and the relative temperature sensitivity (S_r) were calculated by Eqs. (4) and (5) [59,60]:

$$S_a = \left|\frac{d\mathrm{FIR}}{dT}\right| \quad (4)$$

$$S_r = \left|\frac{1}{\mathrm{FIR}} \times \frac{d\mathrm{FIR}}{dT}\right| \times 100\% \quad (5)$$

As shown in Fig. 6(e), the absolute sensitivity (S_{a1}) based on FIR_1 shows a monotonic downward trend as the temperature increases from 150 to 450 K, and the obtained maximal value is 0.047 K^{-1} at 150 K. In contrast, as displayed in Fig. 6(f), the relative sensitivity (S_{r1}) increases, and the maximum S_{r1} is 27.65 %·K^{-1} at 450 K, which is much greater than that of most of the recently reported phosphors for temperature sensing listed in Table 1. To the best of our knowledge, this value is almost the highest among reported Eu^{2+} and Eu^{3+} co-doped thermometers. S_{a2} and S_{r2} of FIR_2 depicted in Figs. 6(h) and 6(i) have similar trends as those of FIR_1. The maximal values of which are 0.18 K^{-1} and 14.05 %·K^{-1}, respectively. Although the calculated S_{r2} is slightly lower than S_{r1}, it is still excellent enough for the application of optical thermometers, as shown in Table 1.

Considering that cycling stability is an important parameter for evaluating the performance of optical thermometers, the PL spectra are measured for several cycles within 150–450 K. The I_{455nm}/I_{616nm} and I_{455nm}/I_{701nm} ratios presented in Fig. S12 in the ESM are basically stable over several cycles, which means that the LSBO:0.02$Eu^{2+/3+}$,0.10Li^+ thermometer is reliable and repeatable. Another crucial parameter for evaluating thermometers is the temperature resolution (δT). Based on several consecutive measurements, the minimum values of δT for FIR_1- and FIR_2-based thermometers are determined to be 0.0004 and 0.0007 K, respectively (see Fig. S13 in the ESM). Evidently, the relatively low δT values further suggest the good temperature-sensing performance of the phosphor prepared in this work.

As listed in Table 1, most of the reported Eu^{2+}- and Eu^{3+}-codoped phosphors for optical thermometry are based only on FIR. However, multiple-mode temperature sensing is far more popular than single-mode temperature sensing because multiple modes not only improve the accuracy of detection but also greatly broaden the scope of applications. Therefore, the temperature-dependent fluorescence decay curves of LSBO:0.02$Eu^{2+/3+}$,0.10Li^+ were measured. The decay curves of Eu^{2+} with excitation and emission wavelengths of 345 and 455 nm are shown in Fig. 7(a). Due to the coexistence of the two phases, the double-exponential model is adopted for estimating the lifetime at various temperatures, and the details are provided in Table S13 in the ESM. Clearly, the average lifetime rapidly decreases from 571.05 to 9.44 ns as the temperature increases from 150 to 450 K. Such a large lifetime variation with the temperature implies good potential for applications in temperature sensing. As shown in Fig. S14 and Table S14 in the ESM, the decay time of Eu^{3+} hardly changes. Therefore, the FL-mode thermometry applied in this work is based on Eu^{2+}.

The sensing sensitivity of the FL mode can be fitted by the model described in Eq. (6) [72,73]:

Table 1 Comparison of performances of this work with those of reported optical thermometer materials based on FIR, including parameters S_{a-max} and S_{r-max} and temperature range

Material	S_{a-max} (K^{-1})	S_{r-max} (%·K^{-1})	Temperature range (K)	Ref.
LSBO:0.02$Eu^{2+/3+}$,0.10Li^+($5d–4f/^5D_0–^7F_2$)	0.047	27.65	150–450	This work
LSBO:0.02$Eu^{2+/3+}$,0.10Li^+($5d–4f/^5D_0–^7F_4$)	0.18	14.05	150–450	This work
Sc_2O_3:$Eu^{2+/3+}$	—	3.06	77–267	[35]
$Sr_{2.05}Li_{0.9}Si_{0.9}Al_{0.1}O_4F$:$Eu^{2+/3+}$	0.0294	0.83	298–573	[36]
$BaMgP_2O_7$:$Eu^{2+/3+}$	0.0094	0.66	300–520	[37]
$Sr_3P_4O_{13}$:$Eu^{2+/3+}$	0.008	1.06	293–573	[38]
$MgAl_2O_4$:$Eu^{2+/3+}$	0.084	0.83	298–523	[39]
$Ca_9Mg_{1.5}(PO_4)_7$:$Eu^{2+/3+}$	0.064	1.192	293–473	[61]
$Ca_9Zn_{1.5}(PO_4)_7$:$Eu^{2+/3+}$	0.0034	1.4	293–473	[62]
$SrAl_2Si_2O_8$:$Eu^{2+/3+}$	0.056	0.30	303–583	[63]
$CaYGaO_4$:$Eu^{2+/3+}$	0.04	3.68	300–570	[64]
$CaBPO_5$:$Eu^{2+/3+}$	0.0184	3.444	303–403	[65]
$Ca_9NaZn(PO_4)_7$:Eu^{2+}	0.0228	0.81	298–498	[30]
$GdNbO_4$:Bi^{3+},Eu^{3+}	0.0367	3.81	303–523	[66]
Ca_2ScSbO_6:Bi^{3+},Eu^{3+}	0.0996	2.002	293–573	[67]
$Na_2Y_2TeB_2O_{10}$:Tb^{3+}	0.0102	5.74	300–475	[68]
$Ba_3(VO_4)_2$:Sm^{3+}	0.039	2.24	303–463	[69]
$Ca_2TbSn_2Al_3O_{12}$:Sm^{3+}	0.15	0.50	300–550	[58]
$Lu_2SrAl_4SiO_{12}$:Cr^{3+},Nd^{3+}	—	1.43	303–483	[57]
$K_7ZnSc_2B_{15}O_{30}$:Mn^{2+}	0.0311	1.84	300–520	[70]
K_2NaScF_6:Yb^{3+},Mn^{2+}	0.018	0.525	298–573	[71]

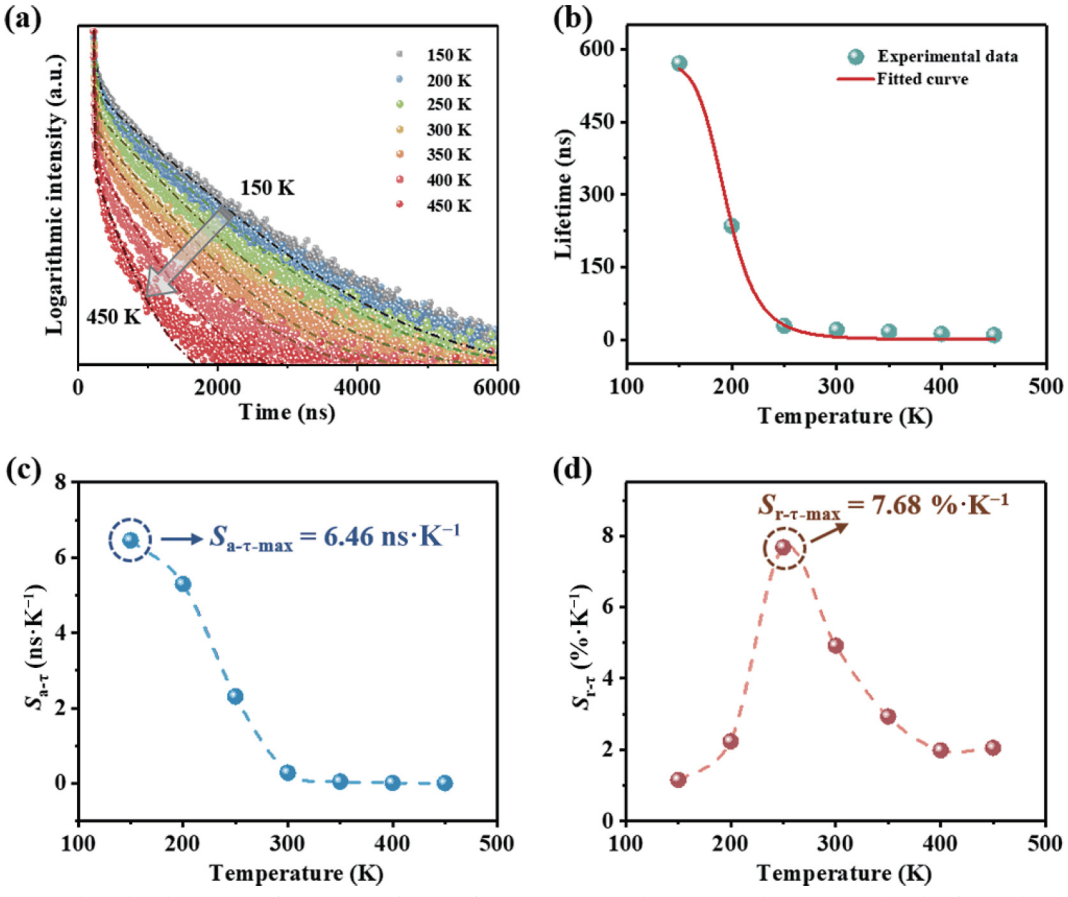

Fig. 7 (a) Temperature-dependent decay curves of LSBO:0.02$Eu^{2+/3+}$,0.10Li^+ from 150 to 450 K with excitation and emission wavelengths of 345 and 455 nm, respectively. (b) Calculated lifetime at different temperatures and fitted curve, (c) calculated $S_{a-\tau}$ values, and (d) calculated $S_{r-\tau}$ values.

$$\tau(T) = \frac{\tau_0}{1 + D\exp\left(-\frac{\Delta E}{kT}\right)} \tag{6}$$

where τ_0, D, ΔE, and k are the lifetime at the initial temperature, the constant, the thermal activation energy, and the Boltzmann constant, respectively. The relationship between τ and T can be fitted as $\tau(T) = \frac{571.05}{1 + 473351.71\times\exp\left(-\frac{2544.53}{kT}\right)}$, and is plotted in Fig. 7(b). A method similar to that of FIR is adopted to calculate the absolute ($S_{a-\tau}$) and relative sensitivity ($S_{r-\tau}$) of the FL mode with Eqs. (7) and (8) [74]:

$$S_{a-\tau} = \left|\frac{d\tau}{dT}\right| \tag{7}$$

$$S_{r-\tau} = \left|\frac{1}{\tau}\times\frac{d\tau}{dT}\right| \times 100\% \tag{8}$$

As shown in Figs. 7(c) and 7(d), $S_{a-\tau}$ shows a gradually decreasing trend, but $S_{r-\tau}$ first increases and then decreases. The maximal values of $S_{a-\tau}$ and $S_{r-\tau}$ are 6.46 ns·K^{-1} at 150 K and 7.68 %·K^{-1} at 250 K, respectively. Compared with some reported optical thermometer materials based on FL, such as Gd_2ZnTiO_6:Mn^{4+} with a maximum $S_{r-\tau}$ of 2.43 %·K^{-1} and $InTaO_4$:Cr^{3+} with a maximum of 2.27 %·K^{-1} [73,75], the parameters of higher $S_{r-\tau}$ and wider temperature range of LSBO:0.02$Eu^{2+/3+}$,0.10Li^+ show obvious advantages. Several measurements of FL at 250 K were conducted to calculate δT, and the minimum value was determined to be 0.018 K, as depicted in Fig. S15 in the ESM. The sufficiently low δT suggested the good reliability of the LSBO:0.02$Eu^{2+/3+}$,0.10Li^+ thermometer.

Considering the crucial parameters based on both the fluorescence intensity ratio and lifetime, including S_{r-max}, $S_{r-\tau-max}$, and temperature range. A comparison of this work with some recent reports is summarized in Table 2. Clearly, both S_{r-max} and $S_{r-\tau-max}$ of this work are evidently higher than those of the investigated reports, and the temperature range of this work is also relatively wide. Figure 8 distinctly shows the superiority of this work over the reports listed in Table 2. The short lines indicating S_{r-max} and $S_{r-\tau-max}$ of this work are located on the far right, and the temperature sensing range described by the column is relatively wider, especially in the region below room temperature, which evidently illustrates the higher S_{r-max} and $S_{r-\tau-max}$ and appropriate thermometry range of this work. Therefore, LSBO:0.02$Eu^{2+/3+}$,0.10Li^+ is supposed to have good potential for applications in multiple-mode optical thermometers.

4 Conclusions

In summary, a multiple-mode optical thermometer was successfully realized in which dual-emitting Eu^{2+} and Eu^{3+} co-existed $LaSc_3(BO_3)_4$ with Li^+ as the charge compensation agent. The phase transition from α to β with the doping of $Eu^{2+/3+}$ or Li^+ was confirmed by the XRD patterns, and the relative percentages of the two phases were determined with XRD refinement. ΔE_{tot} and ΔE_{ave} of the system energy were calculated via first-principles calculations to understand the phase transition process. The

Table 2 Comparison of performances of reported multiple-mode optical thermometer materials with LSBO:0.02$Eu^{2+/3+}$,0.10Li^{+}, including parameters S_{r-max}, $S_{r-\tau-max}$, and temperature range

Material	FIR-based		FL-based		Ref.
	S_{r-max} (%·K^{-1})	Temperature range (K)	$S_{r-\tau-max}$ (%·K^{-1})	Temperature range (K)	
LSBO:0.02$Eu^{2+/3+}$,0.10Li^{+}	27.65[a]/14.05[b]	150–450	7.68	150–450	This work
$Li_4SrCa(SiO_4)_2$:Eu^{2+}	3.18	303–473	15.0	303–573	[76]
$Y_2Ti_2O_7$:Bi^{3+}	3.52	78–378	3.53	78–298	[77]
Sr_2InSbO_6:Sm^{3+}	10.9	298–523	2.15	298–523	[78]
$La_2Mg_{1.33}Ta_{0.67}O_6$:$Mn^{4+}$,$Eu^{3+}$	2.72[c]/2.49[d]	298–448	3.36[c]/3.42[d]	298–448	[79]
$CaGdMgSbO_6$:Mn^{4+},Sm^{3+}	1.54	298–573	1.23	298–573	[80]
La_2MgGeO_6:Bi^{3+},Eu^{3+}	2.389	293–473	4.09	293–433	[81]
$Ba_{0.5}Sr_{0.5}Al_{11.93}O_{19}$:$Mn^{2+}$,$Mn^{4+}$	4.37	293–406	4.48	293–393	[82]
$SrLaLiTeO_6$:Mn^{4+},Dy^{3+}	1.60[e]/1.44[f]	298–673	1.59[e]/2.18[f]	298–673	[83]
$BaGd_2O_4$:Bi^{3+},Sm^{3+}	1.105	293–473	1.6621	293–473	[84]
$BaAl_{12}O_{19}$:Eu^{2+},Cr^{3+}	0.259	295–476	0.466	293–563	[85]
$Lu_3Al_5O_{12}$:Ce^{3+},Mn^{4+}	4.37	100–350	3.22	100–350	[86]
La_2MgTiO_6:Pr^{3+},Dy^{3+}	2.357	298–548	1.814	298–548	[72]

Note: [a]Result based on FIR_1 ($5d–4f/^5D_0–^7F_2$); [b]result based on FIR_2 ($5d–4f/^5D_0–^7F_4$); [c]excitation wavelength is 300 nm; [d]excitation wavelength is 465 nm; [e]excitation wavelength is 351 nm; [f]excitation wavelength is 453 nm.

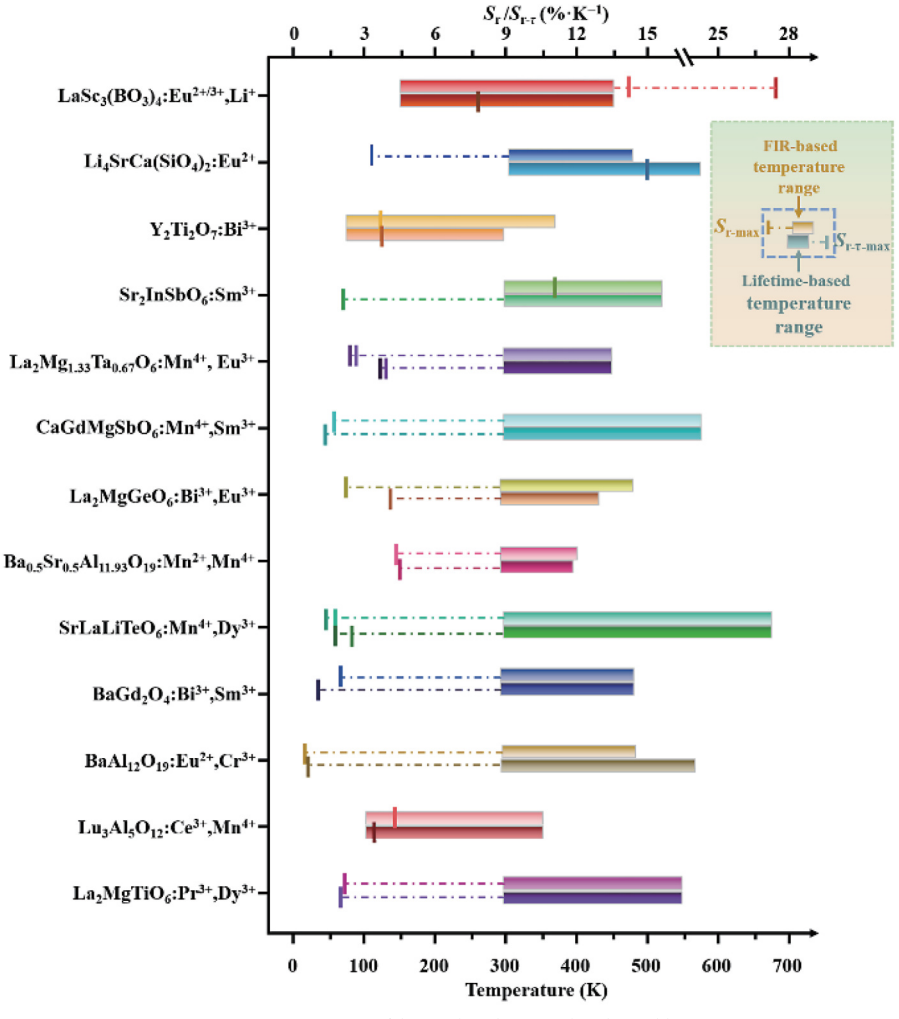

Fig. 8 Comparison of this work with reports listed in Table 2.

activators of Eu^{2+} and Eu^{3+} tend to occupy the sites of La^{3+} rather than those of Sc^{3+} based on the D_r and ΔE values. The relative percentages of Eu^{2+} and Eu^{3+} were determined by XANES, and the corresponding values for LSBO:0.02$Eu^{2+/3+}$ and 0.10Li^{+} were 20.57% and 79.43%, respectively. Both the characteristic emissions of Eu^{2+} and Eu^{3+} can be observed in the PL spectra, and no obvious

energy transfer between the two activators has been discovered. The variations in the luminescence of the $4f^65d^1$–$4f^7$ transition of Eu^{2+} were carefully analyzed, and the positive effects of the appropriate charge compensation agent on the luminescence of LSBO:0.02$Eu^{2+/3+}$ were confirmed. The observed redshift with increasing doping concentrations of $Eu^{2+/3+}$ and Li^+ can be explained by the changing pressure exerted on the [EuO_6] octahedra. According to the refinements of temperature-dependent XRD, the crystal structure and the phase percentage are hardly influenced by the temperature. Therefore, further investigations of temperature sensing have been conducted using temperature-dependent PL and lifetime measurements. Due to the opposite thermal quenching properties between Eu^{2+} and Eu^{3+} under excitation at 307 nm, a shift in the emission color from cyan to blue and pink can be distinctly observed. Two temperature sensing modes based on FIR_1 (5d–4f/$^5D_0$–$^7F_2$) and FIR_2 (5d–4f/$^5D_0$–$^7F_4$) were realized in the temperature range of 150–450 K, with maximal relative sensitivities of 27.65 and 14.05 %·K^{-1} at 450 K, respectively. To the best of our knowledge, the former is almost the highest among reported Eu^{2+} and Eu^{3+} co-doped thermometers. The FL-based method has also been used to detect temperatures in the same temperature range, with the highest relative sensitivity of 7.68 %·K^{-1} at 250 K. The minimum temperature resolutions are 0.0004, 0.0007, and 0.018 K, respectively. The cycling measurements of the PL spectra showed that the LSBO:0.02$Eu^{2+/3+}$,0.10Li^+ thermometer is reliable and repeatable. By comparing the reported multiple-mode optical thermometer materials, this work is shown to have significant superiorities and promising potential for application in multiple-mode optical thermometers.

Acknowledgements

This work was financially supported by the National Natural Science Foundation of China (Nos. 51972347 and 21771195).

Declaration of competing interest

The authors have no competing interests to declare that are relevant to the content of this article.

Electronic Supplementary Material

Supplementary material is available in the online version of this article at https://doi.org/10.26599/JAC.2024.9220901.

References

[1] Wang XD, Wolfbeis OS, Meier RJ. Luminescent probes and sensors for temperature. *Chem Soc Rev* 2013, **42**: 7834–7869.

[2] Brites CDS, Balabhadra S, Carlos LD. Lanthanide-based thermometers: At the cutting-edge of luminescence thermometry. *Adv Opt Mater* 2019, **7**: 1801239.

[3] Suo H, Zhao XQ, Zhang ZY, *et al.* Rational design of ratiometric luminescence thermometry based on thermally coupled levels for bioapplications. *Laser Photonics Rev* 2021, **15**: 2000319.

[4] Ansari AA, Parchur AK, Nazeeruddin MK, *et al.* Luminescent lanthanide nanocomposites in thermometry: Chemistry of dopant ions and host matrices. *Coordin Chem Rev* 2021, **444**: 214040.

[5] Xue J, Li L, Runowski M, *et al.* Precisely manipulating the self-reduction of manganese in $MgGa_2O_4$ through lithium incorporation for optical thermometry and anti-counterfeiting. *Adv Opt Mater* 2023, **11**: 2300600.

[6] Chen DH, Haldar R, Wöll C. Stacking lanthanide-MOF thin films to yield highly sensitive optical thermometers. *ACS Appl Mater Inter* 2023, **15**: 19665–19671.

[7] Wang Q, Liao M, Lin QM, *et al.* A review on fluorescence intensity ratio thermometer based on rare-earth and transition metal ions doped inorganic luminescent materials. *J Alloys Compd* 2021, **850**: 156744.

[8] Zhong L, Jiang S, Wang XH, *et al.* Dual-mode optical thermometry based on intervalence charge transfer excitations in Tb^{3+}/Pr^{3+} co-doped $CaNb_2O_6$ phosphors. *Ceram Int* 2022, **48**: 30005–30011.

[9] van Swieten TP, Yu D, Yu T, *et al.* A Ho^{3+}-based luminescent thermometer for sensitive sensing over a wide temperature range. *Adv Opt Mater* 2021, **9**: 2001518.

[10] Liu X, Mi X, Guo Y, *et al.* Highly sensitive and near-infrared excitable optical thermometer based on $CaGdAl_3O_7$:Tm^{3+},Yb^{3+},Zn^{2+}. *J Alloys Compd* 2022, **929**: 167240.

[11] Xue J, Yu Z, Noh HM, *et al.* Designing multi-mode optical thermometers via the thermochromic $LaNbO_4$:Bi^{3+}/Ln^{3+} (Ln = Eu, Tb, Dy, Sm) phosphors. *Chem Eng J* 2021, **415**: 128977.

[12] Zhou LY, Chen YL, Shen YY, *et al.* Designing optical thermometers using down/upconversion $Ca_{14}Al_{10}Zn_6O_{35}$:Ti^{4+},Eu^{3+}/Yb^{3+},Er^{3+} thermosensitive phosphors. *Inorg Chem* 2022, **61**: 10667–10677.

[13] Zhang H, Gao ZY, Li GG, *et al.* A ratiometric optical thermometer with multi-color emission and high sensitivity based on double perovskite $LaMg_{0.402}Nb_{0.598}O_3$:$Pr^{3+}$ thermochromic phosphors. *Chem Eng J* 2020, **380**: 122491.

[14] Ding H, Lv GQ, Cai X, *et al.* An optoelectronic thermometer based on microscale infrared-to-visible conversion devices. *Light Sci Appl* 2022, **11**: 130.

[15] Chen ZL, Du SM, Zhu KM, *et al.* Mn^{4+}-activated double-perovskite-type Sr_2LuNbO_6 multifunctional phosphor for optical probing and lighting. *ACS Appl Mater Inter* 2023, **15**: 28193–28203.

[16] Peng M, Kaczmarek AM, van Hecke K. Ratiometric thermometers based on rhodamine B and fluorescein dye-incorporated (nano) cyclodextrin metal–organic frameworks. *ACS Appl Mater Inter* 2022, **14**: 14367–14379.

[17] Xu CW, Li CX, Deng DG, *et al.* A dual-mode optical thermometer with high sensitivity based on $BaAl_{12}O_{19}$:Sm^{2+}/$SrAl_{12}O_{19}$:Sm^{3+} solid solution phosphors. *Inorg Chem* 2022, **61**: 7989–7999.

[18] Wei RF, Lu FM, Wang L, *et al.* Splendid four-mode optical thermometry design based on thermochromic $Cs_3GdGe_3O_9$:Er^{3+} phosphors. *J Mater Chem C* 2022, **10**: 9492–9498.

[19] Yuan J, Zhao GS, Ren SQ, *et al.* Multimode fluorescence intensity ratio thermometer based on synergistic luminescence from Eu^{3+} to Mn^{4+} of $SrTiO_3$:Eu^{3+}–$uTiOt_3$:Mn^{4+} nanocomposites. *Ceram Int* 2023, **49**: 17699–17708.

[20] Zhang XG, Zhu ZP, Guo ZY, *et al.* A ratiometric optical thermometer with high sensitivity and superior signal discriminability based on $Na_3Sc_2P_3O_{12}$:Eu^{2+},Mn^{2+} thermochromic phosphor. *Chem Eng J* 2019, **356**: 413–422.

[21] Fan ZT, Bi SL, Seo HJ. Tunable emission via dual-site occupancy in $Ba_2CaB_2Si_4O_{14}$:Bi^{3+},Sm^{3+} phosphors. *J Alloys Compd* 2022, **916**: 165347.

[22] Jahanbazi F, Mao YB. Recent advances on metal oxide-based luminescence thermometry. *J Mater Chem C* 2021, **9**: 16410–16439.

[23] Tian Y, Tian Y, Huang P, *et al.* Effect of Yb^{3+} concentration on upconversion luminescence and temperature sensing behavior in Yb^{3+}/Er^{3+} co-doped $YNbO_4$ nanoparticles prepared via molten salt route. *Chem Eng J* 2016, **297**: 26–34.

[24] Suo H, Zhao XQ, Zhang ZY, *et al.* Ultra-sensitive optical nano-thermometer $LaPO_4$:Yb^{3+}/Nd^{3+} based on thermo-enhanced NIR-to-NIR emissions. *Chem Eng J* 2020, **389**: 124506.

[25] Liu W, Zhao D, Zhang RJ, *et al.* Fluorescence lifetime-based luminescent thermometry material with lifetime varying over a factor of 50. *Inorg Chem* 2022, **61**: 16468–16476.

[26] Chen JY, Chen JQ, Li LJ, *et al.* A four-mode high-sensitive optical thermometer based on $Ca_3LiZnV_3O_{12}$:Sm^{3+} phosphors. *Mater Today Chem* 2023, **29**: 101409.

[27] Chen JQ, Chen JY, Zhang WN, *et al.* Three-mode optical thermometer based on $Ca_3LiMgV_3O_{12}$:Sm^{3+} phosphors. *Ceram Int* 2023, **49**: 16252–16259.

[28] Ayachi F, Saidi K, Dammak M, *et al.* Dual-mode luminescence of Er^{3+}/Yb^{3+} codoped $LnP_{0.5}V_{0.5}O_4$ (Ln = Y, Gd, La) for highly sensitive optical nanothermometry. *Mater Today Chem* 2023, **27**: 101352.
[29] Mi RY, Liu YG, Mei LF, *et al.* Highly-efficient cyan-emitting phosphor enabling high-color-quality lighting and transparent anticounterfeiting. *Chem Eng J* 2023, **457**: 141377.
[30] Zhang D, Zheng BF, Zheng ZB, *et al.* Multifunctional $Ca_9NaZn_{1-y}Mg_y(PO_4)_7:Eu^{2+}$ phosphor for full-spectrum lighting, optical thermometry and pressure sensor applications. *Chem Eng J* 2022, **431**: 133805.
[31] Xiang Y, Liu ZY, Gao Y, *et al.* Novel double perovskite $Ca_2Gd_{0.5}Nb_{1-x}W_{5x/6}O_6$:0.5$Eu^{3+}$ red phosphors with excellent thermal stability and high color purity for white LEDs. *Chem Eng J* 2023, **456**: 140901.
[32] Xiang YF, Zhang HZ, Li JP, *et al.* Layered structure-induced quenching delay toward highly efficient and thermally stable red emission in Eu^{3+}-activated borotellurate phosphors. *J Mater Chem C* 2024, **12**: 2037–2047.
[33] Zhu J, Yang TS, Li H, *et al.* Cationic composition engineering in double perovskite $XLaLiTeO_6$: Eu^{3+} (X = Ba, Sr, Ca, and Mg) toward efficient and thermally stable red luminescence for domestic white-LEDs. *J Mater Chem C* 2023, **11**: 11017–11026.
[34] Binnemans K. Interpretation of europium(III) spectra. *Coordin Chem Rev* 2015, **295**: 1–45.
[35] Pan Y, Xie XJ, Huang QW, *et al.* Inherently Eu^{2+}/Eu^{3+} codoped Sc_2O_3 nanoparticles as high-performance nanothermometers. *Adv Mater* 2018, **30**: 1705256.
[36] Huang S, Shang MM, Yan Y, *et al.* Regulation of local site structures to stabilize mixed-valence $Eu^{2+/3+}$ under a reducing atmosphere for multicolor photoluminescence. *Inorg Chem* 2022, **61**: 1756–1764.
[37] Li S, Qiu ZX, Mo YH, *et al.* Self-reduction-induced $BaMgP_2O_7:Eu^{2+/3+}$: A multi-stimuli-responsive phosphor for X-ray detection, anti-counterfeiting and optical thermometry. *Dalton T* 2022, **51**: 6622–6630.
[38] Yu H, Su WT, Chen LF, *et al.* Excellent temperature sensing characteristics of europium ions self-reduction $Sr_3P_4O_{13}$ phosphors for ratiometric luminescence thermometer. *J Alloys Compd* 2019, **806**: 833–840.
[39] Kolesnikov IE, Afanaseva EV, Kurochkin MA, *et al.* Mixed-valent $MgAl_2O_4:Eu^{2+}/Eu^{3+}$ phosphor for ratiometric optical thermometry. *Physica B* 2022, **624**: 413456.
[40] Wang Y, Xiao J, Zhu HY, *et al.* Structural phase transition in monolayer $MoTe_2$ driven by electrostatic doping. *Nature* 2017, **550**: 487–491.
[41] Ananias D, Paz FAA, Yufit DS, *et al.* Photoluminescent thermometer based on a phase-transition lanthanide silicate with unusual structural disorder. *J Am Chem Soc* 2015, **137**: 3051–3058.
[42] Yang N, Li JH, Zhang ZW, *et al.* Delayed concentration quenching of luminescence caused by Eu^{3+}-induced phase transition in $LaSc_3(BO_3)_4$. *Chem Mater* 2020, **32**: 6958–6967.
[43] Toby BH. EXPGUI, a graphical user interface for GSAS. *J Appl Crystallogr* 2001, **34**: 210–213.
[44] Blöchl PE. Projector augmented-wave method. *Phys Rev B* 1994, **50**: 17953–17979.
[45] Perdew JP, Burke K, Ernzerhof M. Generalized gradient approximation made simple. *Phys Rev Lett* 1996, **77**: 3865–3868.
[46] Kresse G, Furthmüller J. Efficiency of *ab-initio* total energy calculations for metals and semiconductors using a plane-wave basis set. *Com Mater Sci* 1996, **6**: 15–50.
[47] Kuz'micheva GM, Mukhin BV, Kuz'min OV, *et al.* X-ray diffraction study of the crystals $LaSc_3(BO_3)_4$ activated with chromium and neodymium ions. *Zh Neorg Khim* 1996, **41**: 1605–1611.
[48] He MY, Wang G, Lin ZB, *et al.* Structure of medium temperature phase β-$LaSc_3(BO_3)_4$ crystal. *Mater Res Innov* 1999, **2**: 345–348.
[49] Wang G, He MY, Chen WZ, *et al.* Structure of low temperature phase γ-$LaSc_3(BO_3)_4$ crystal. *Mater Res Innov* 1999, **2**: 341–344.
[50] Shannon RD. Revised effective ionic radii and systematic studies of interatomic distances in halides and chalcogenides. *Acta Crystallogr A* 1976, **A32**: 751–767.
[51] Qiao JW, Amachraa M, Molokeev M, *et al.* Engineering of $K_3YSi_2O_7$ to tune photoluminescence with selected activators and site occupancy. *Chem Mater* 2019, **31**: 7770–7778.
[52] Yang ZY, Zhao YF, Zhou YY, *et al.* Giant red-shifted emission in $(Sr,Ba)Y_2O_4:Eu^{2+}$ phosphor toward broadband near-infrared luminescence. *Adv Funct Mater* 2021, **32**: 2103927.
[53] Xie GD, Si JY, Li GH, *et al.* Environment-dependent Eu^{2+}-activated $Ba_3CaK(PO_4)_3$ toward white-light emission by chemical cosubstitution of the $(BO_3)^{3-}$ anion group. *Inorg Chem* 2022, **61**: 14845–14856.
[54] Wang JB, Zhou XJ, Xiang GT, *et al.* The explanation of abnormal thermal quenching of the charge transfer band based on thermally coupled levels and applications as temperature sensing probes. *Dalton T* 2022, **51**: 17224–17234.
[55] Zhou XJ, Zhao SC, Li SY, *et al.* Luminescent properties of Eu^{3+}-doped $NaLaCaWO_6$ red phosphors and temperature sensing derived from the excited state of charge transfer band. *J Lumin* 2022, **248**: 118964.
[56] Yang N, Li Z, Zhang ZW, *et al.* A highly thermal-stable red-emitting tantalate phosphor for WLED and multiple-mode optical temperature sensor dual-applications. *Ceram Int* 2024, **50**: 6880–6891.
[57] Zhou LH, Lyu ZY, Sun DS, *et al.* Enhanced thermal stability and energy transfer by crystal-field engineering in a garnet phosphor for thermometry and NIR-LED. *Adv Opt Mater* 2022, **10**: 2201308.
[58] Zhang ZW, Yan J, Zhang QH, *et al.* Enlarging sensitivity of fluorescence intensity ratio-type thermometers by the interruption of the energy transfer from a sensitizer to an activator. *Inorg Chem* 2022, **61**: 16484–16492.
[59] Du P, Tang J, Li W, *et al.* Exploiting the diverse photoluminescence behaviors of $NaLuF_4:xEu^{3+}$ nanoparticles and g-C_3N_4 to realize versatile applications in white light-emitting diode and optical thermometer. *Chem Eng J* 2021, **406**: 127165.
[60] Dong LP, Zhang L, Jia YC, *et al.* $ZnGa_{2-y}Al_yO_4:Mn^{2+},Mn^{4+}$ thermochromic phosphors: Valence state control and optical temperature sensing. *Inorg Chem* 2020, **59**: 15969–15976.
[61] Ruan FP, Deng DG, Wu M, *et al.* Multichannel luminescence of Eu^{2+}/Eu^{3+} co-activated $Ca_9Mg_{1.5}(PO4)_7$ phosphors for self-referencing optical thermometry. *J Lumin* 2019, **213**: 117–126.
[62] Yu H, Ruan FP, Chen LF, *et al.* Dual-emitting Eu^{2+}/Eu^{3+} co-doped $Ca_9Zn_{1.5}(PO_4)_7$ phosphor for self-calibrated optical thermometry. *Opt Mater* 2020, **100**: 109678.
[63] Xue JP, Song MJ, Noh HM, *et al.* Achieving non-contact optical thermometer via inherently Eu^{2+}/Eu^{3+}-activated $SrAl_2Si_2O_8$ phosphors prepared in air. *J Alloys Compd* 2020, **843**: 155858.
[64] Guo HJ, Chen YQ, Wang L, *et al.* Utilizing diametrically opposite thermal quenching luminescence to achieve highly sensitive temperature measurement and anti-counterfeiting. *Inorg Chem Front* 2024, **11**: 799–807.
[65] Meng ZC, Gao Y, Song JA, *et al.* Tetrahedrally coordinated rigid crystal structure enables partial self-reduction of mixed-valence europium for optical thermometric application. *Dalton T* 2023, **52**: 5443–5452.
[66] Xue JP, Noh HM, Choi BC, *et al.* Dual-functional of non-contact thermometry and field emission displays via efficient Bi^{3+}→Eu^{3+} energy transfer in emitting-color tunable $GdNbO_4$ phosphors. *Chem Eng J* 2020, **382**: 122861.
[67] Zhang XB, Xu YH, Wu XD, *et al.* Optical thermometry and multi-mode anti-counterfeiting based on Bi^{3+}/Ln^{3+} and Ln^{3+} doped Ca_2ScSbO_6 phosphors. *Chem Eng J* 2024, **481**: 148717.
[68] Xiang YF, Yang L, Liao CY, *et al.* Thermometric properties of $Na_2Y_2TeB_2O_{10}:Tb^{3+}$ green phosphor based on fluorescence/excitation intensity ratio. *J Adv Ceram* 2023, **12**: 848–860.
[69] Du P, Hua YB, Yu JS. Energy transfer from VO_4^{3-} group to Sm^{3+} ions in $Ba_3(VO_4)_2:3xSm^{3+}$ microparticles: A bifunctional platform for simultaneous optical thermometer and safety sign. *Chem Eng J* 2018, **352**: 352–359.

[70] Fu Y, Li C, Zhang F, *et al.* Site preference and the optical thermometry strategy by different temperature response from two sites environment of Mn^{2+} in $K_7ZnSc_2B_{15}O_{30}$. *Chem Eng J* 2021, **409**: 128190.
[71] Liu DX, Zeng CY, Wang J, *et al.* Site preference induced dual-wavelength Mn^{2+} upconversion in K_2NaScF_6:Yb^{3+},Mn^{2+} and its application in temperature sensing. *Adv Opt Mater* 2024, **12**: 2302819.
[72] Zhang H, Liang YJ, Yang H, *et al.* Highly sensitive dual-mode optical thermometry in double-perovskite oxides via Pr^{3+}/Dy^{3+} energy transfer. *Inorg Chem* 2020, **59**: 14337–14346.
[73] Zheng T, Luo L, Du P, *et al.* Highly-efficient double perovskite Mn^{4+}-activated Gd_2ZnTiO_6 phosphors: A bifunctional optical sensing platform for luminescence thermometry and manometry. *Chem Eng J* 2022, **446**: 136839.
[74] Xie CY, Wang P, Lin Y, *et al.* Temperature-dependent luminescence of a phosphor mixture of Li_2TiO_3:Mn^{4+} and Y_2O_3:Dy^{3+} for dual-mode optical thermometry. *J Alloys Compd* 2020, **821**: 153467.
[75] Qiu LT, Wang P, Mao JS, *et al.* Cr^{3+}-doped $InTaO_4$ phosphor for multi-mode temperature sensing with high sensitivity in a physiological temperature range. *Inorg Chem Front* 2022, **9**: 3187–3199.
[76] Wu M, Deng DG, Ruan FP, *et al.* A spatial/temporal dual-mode optical thermometry based on double-sites dependent luminescence of $Li_4SrCa(SiO_4)_2$:Eu^{2+} phosphors with highly sensitive luminescent thermometer. *Chem Eng J* 2020, **396**: 125178.
[77] Wang XL, Jahanbazi F, Wei JL, *et al.* Charge transfer-triggered Bi^{3+} near-infrared emission in $Y_2Ti_2O_7$ for dual-mode temperature sensing. *ACS Appl Mater Inter* 2022, **14**: 36834–36844.
[78] Xia WD, Li L, Hua YB, *et al.* Realizing dual-mode luminescent thermometry with excellent sensing sensitivity in single-phase samarium(III)-doped antimonite phosphors. *J Alloys Compd* 2022, **917**: 165435.
[79] Song MJ, Wang LT, Wang JC, *et al.* Constructing double perovskite Eu^{3+}/Mn^{4+}-codoped $La_2Mg_{1.33}Ta_{0.67}O_6$ phosphors for high sensitive dual-mode optical thermometers. *J Lumin* 2022, **252**: 119347.
[80] Liao JS, Wang MH, Kong LY, *et al.* Dual-mode optical temperature sensing behavior of double-perovskite $CaGdMgSbO_6$:Mn^{4+}/Sm^{3+} phosphors. *J Lumin* 2020, **226**: 117492.
[81] Chen YL, Shen YY, Zhou LY, *et al.* Temperature-dependent luminescence of Bi^{3+},Eu^{3+} co-activated La_2MgGeO_6 phosphor for dual-mode optical thermometry. *J Lumin* 2022, **249**: 118995.
[82] Zhu YT, Li CX, Deng DG, *et al.* A high-sensitivity dual-mode optical thermometry based on one-step synthesis of Mn^{2+}:$BaAl_{12}O_{19}$–Mn^{4+}:$SrAl_{12}O_{19}$ solid solution phosphors. *J Alloys Compd* 2021, **853**: 157262.
[83] Wu ZJ, Li L, Tian G, *et al.* High-sensitivity and wide-temperature-range dual-mode optical thermometry under dual-wavelength excitation in a novel double perovskite tellurate oxide. *Dalton T* 2021, **50**: 11412–11421.
[84] Fu J, Zhou LY, Chen YL, *et al.* Dual-mode optical thermometry based on Bi^{3+}/Sm^{3+} co-activated $BaGd_2O_4$ phosphor with tunable sensitivity. *J Alloys Compd* 2022, **897**: 163034.
[85] Zhu YT, Li CX, Deng DG, *et al.* High-sensitivity based on Eu^{2+}/Cr^{3+} co-doped $BaAl_{12}O_{19}$ phosphors for dual-mode optical thermometry. *J Lumin* 2021, **237**: 118142.
[86] Chen YB, He J, Zhang XG, *et al.* Dual-mode optical thermometry design in $Lu_3Al_5O_{12}$:Ce^{3+}/Mn^{4+} phosphor. *Inorg Chem* 2020, **59**: 1383–1392.